

Article

A Novel Hybrid Control Strategy and Dynamic Performance Enhancement of a 3.3 kW GaN–HEMT-Based iL^2C Resonant Full-Bridge DC–DC Power Converter Methodology for Electric Vehicle Charging Systems

Rajanand Patnaik Narasipuram *  and Subbarao Mopidevi

Department of Electrical and Electronics Engineering, Vignan's Foundation for Science Technology and Research, Guntur 522213, India

* Correspondence: rajanand.ee@gmail.com or rajanand.patnaik@ieee.org



Citation: Narasipuram, R.P.; Mopidevi, S. A Novel Hybrid Control Strategy and Dynamic Performance Enhancement of a 3.3 kW GaN–HEMT-Based iL^2C Resonant Full-Bridge DC–DC Power Converter Methodology for Electric Vehicle Charging Systems. *Energies* **2023**, *16*, 5811. <https://doi.org/10.3390/en16155811>

Academic Editors:
Sreedhar Madichetty and
Abdelkader El Kamel

Received: 15 June 2023
Revised: 31 July 2023
Accepted: 3 August 2023
Published: 4 August 2023



Copyright: © 2023 by the authors. Licensee MDPI, Basel, Switzerland. This article is an open access article distributed under the terms and conditions of the Creative Commons Attribution (CC BY) license (<https://creativecommons.org/licenses/by/4.0/>).

Abstract: The conventional resonant inductor–inductor–capacitor (L^2C) DC–DC converters have the major drawbacks of poor regulation, improper current sharing, load current ripples, conduction losses, and limiting the power levels to operate at higher loads for electric vehicle (EV) charging systems. To address the issues of the L^2C converter, this paper proposes an interleaved inductor–inductor–capacitor (iL^2C) full-bridge (FB) DC–DC converter as an EV charger with wide input voltage conditions. It comprises two L^2C converters operating in parallel on the primary side with 8-GaN switches and maintains the single rectifier circuit on the secondary side as common. Further, it introduces the hybrid control strategy called variable frequency + phase shift modulation (VFPSM) technique for iL^2C with a constant voltage charging mode operation. The design requirements, modeling, dynamic responses, and operation of an iL^2C converter with a controller are discussed. The analysis of the proposed concept designed and simulated with an input voltage of $400 V_{in}$ at a load voltage of $48 V_0$ presented at different load conditions, i.e., full load (3.3 kW), half load (1.65 kW), and light load (330 W). The dynamic performances of the converter during line and load regulations are presented at assorted input voltages. In addition, to analyze the controller and converter performance, the concept was validated experimentally for wide input voltage applications of $300\text{--}500 V_{in}$ with a desired output of $48 V_0$ at full load condition, i.e., 3.3 kW and the practical efficiency of the iL^2C converter was 98.2% at full load.

Keywords: electric vehicle charger; charging system; L^2C resonant converter; interleaved L^2C resonant converter; full-bridge; hybrid control strategy; variable frequency + phase shift modulation; constant voltage mode; wide band gap; gallium nitride

1. Introduction

These days, conventional internal combustion engines (ICEs) are becoming saturated due to a deficiency of fossil resources, and the environment is polluted with toxic gases, carbon emissions, and drastic climate changes. Considering this, there is a global call for implementing clean energy transportation to safeguard against climatic changes. Recently, EVs as an eco-friendly power source have gained significant popularity, with the promising objective of replacing ICEs and reducing CO_2 emissions [1]. Electrifying the transportation sector with battery electric vehicles (BEVs), fuel-cell electric vehicles (FCEVs), hybrid electric vehicles (HEVs), ultra-capacitor electric vehicles (UCEVs), supercapacitor electric vehicles (SCEVs), and plugin hybrid electric vehicles (PHEVs) can significantly reduce emission rates. The industry is advancing toward the adoption of electric vehicles achieve net-zero emissions by 2030 in Europe and 2050 in India. Due to the increasing demand for EVs, the development of charging topologies that are more reliable and efficient is essential. There are several charging topologies in terms of power electronics architectures

for applications such as solar, EV, etc., with optimizing methods discussed in [2–4]. The typical block diagram of a charging architecture is shown in Figure 1.

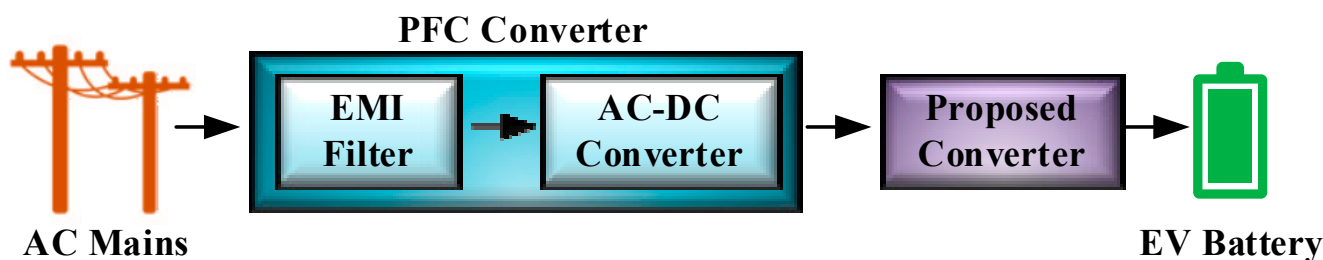


Figure 1. Typical block diagram of an EV charging power conversion system.

During the past decade, much research has been conducted on a wide variety of DC–DC converters for various applications such as electric vehicles, photovoltaics, and fuel cell applications [5,6]. Many L^2C resonant converters are gaining popularity due to their merits of zero voltage switching (ZVS) operation on the primary side at all load conditions and zero current switching (ZCS) operation on the secondary side with synchronous rectification, wide voltage gain, the ability to provide soft switching characteristics, and high power density with high switching frequency capability [7,8]. Additionally, the dv/dt at the primary side of the circuit is smaller due to the L^2C converter’s lower turn-off current, resulting in lower electromagnetic interference (EMI) [9,10].

A typical L^2C Resonant FB DC–DC converter is shown in Figure 2. It consists of a series resonant tank, which includes an inductor L_r and capacitor C_r in series with a high-frequency transformer to provide sufficient galvanic isolation, and a parallel inductance also available in the resonant tank, which is called magnetizing inductance L_m to form the resonant network [11]. For wide voltage gain applications, the switching frequency f_s must vary in a wide range, and the designer needs to take care of the ZVS function because it may be lost if the switching frequency is too low. The effect of the junction capacitance C_j , as discussed in [12], of secondary side rectifying diodes causes poor voltage control when f_s exceeds the resonant frequency f_r . The magnetic component size is constrained by the low switching frequency f_s . As a result, designing an L^2C converter with a broad output voltage range poses considerable challenges, and performance degrades rapidly as f_s deviates from f_r [13,14]. In general, there are three different modes of operation in a L^2C converter, including above resonance, below resonance, and at resonance. During all these modes of operation, the regulation control on the ZCS region is fully achieved, but in the case of the ZVS region, there is poor performance in regulation at different load conditions with variable input voltages. Additionally, to utilize the L^2C converter as an EV charger, there are certain limitations such as increasing the load capacity to operate at higher power levels, current and voltage ripples at the output side causing damage to the product, and the efficiency at high power levels being low [15].

To overcome the drawbacks of the L^2C converter, this paper considered a two-stage interleaved L^2C (iL²C) converter. Due to the resonant tank design of L^2C , the load capacity is limited, which results in an increased circulating current and thereby lower efficiency. Using iL²C this problem can be solved by adding the L^2C in parallel to double the load capacity [16]. Additionally, at high current applications, the major power loss component is the transformer, which has eddy current loss (AC loss) and winding losses of copper resistance (DC loss), and splitting the circuit transformer current reduces the losses of AC and DC. Using the interleaving technique reduces the current ripples [17].

To date, numerous control strategies have been defined to provide soft switching, tight regulation, and reduce the circulating current [18,19]. These methods are operated by adding the transformer current via injecting zero-voltage on the primary or secondary side, and this can also be obtained by changing the phase shifting method. Some papers suggested [18,19] that different control strategies can be used at different regions such as $f_s < f_r$, $f_s = f_r$ and $f_s > f_r$ but this affects the regulation. Rather than using the zero-voltage

sequence method and other techniques mentioned to extend the soft switching region [20], this paper proposes a hybrid control strategy called the VFPSM technique for iL^2C FB converter. It is based on switching at a predefined current value. The proposed scheme allows either a ZCS or ZVS depending on how the designer chooses the switching current level. In addition, it also minimizes the root mean square (RMS) current in the transformer by fixing the predefined value of reactive current [21,22]. Hence, it provides an additional advantage to the controller concerning conventional phase shift modulation between the primary and secondary of transformer [23,24]. Additionally, with this method, soft switching can be achieved with low conduction losses, and proper load and line regulations are conducted and increase the system's efficiency. Meanwhile, there are certain limitations, such as its complicated design, which require proper tuning of control parameters [25,26].

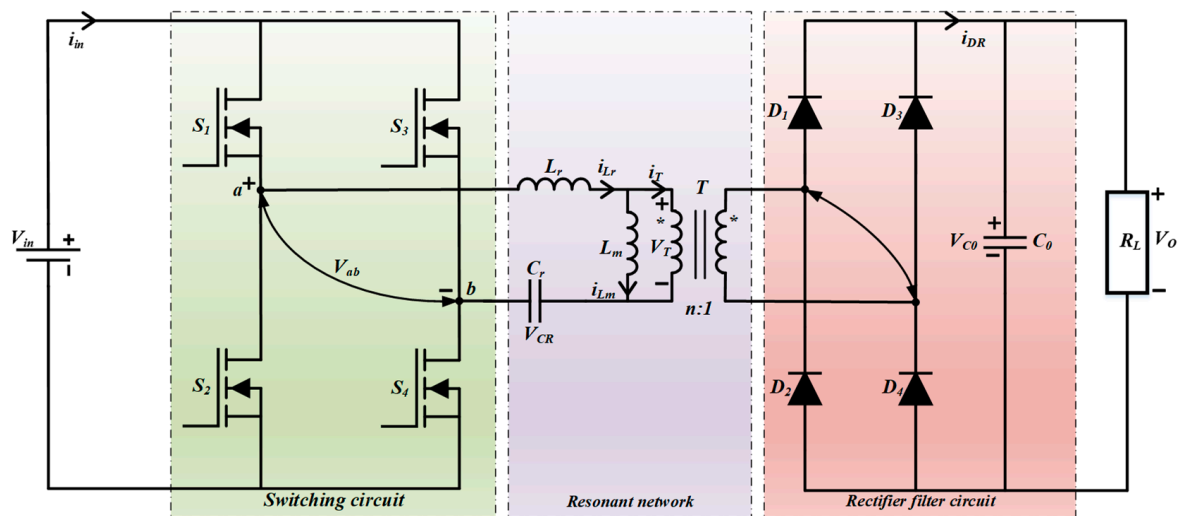


Figure 2. L^2C resonant FB DC–DC power converter.

Furthermore, this paper also sheds light on the GaN-HEMT-based technology's implementation on the proposed system [27,28]. The superior characteristics of GaN technology compared to Si (silicon), such as a wideband gap, reliability, packaging, heating, efficiency, and operating at high power density with frequency, serve as major advantages of GaN technology [29]. To reduce the losses at high power operation, a lower R_{dson} is required to improve the efficiency of the entire system to confer more reliable operation at higher switching speeds [30].

The main research contributions of this paper are summarized below:

1. Modeling of iL^2C converter topology was carried out to enhance the load capacity, reduce the current ripples, and reduce the circulating current;
2. A hybrid control strategy was introduced across all operating modes to improve the regulation, minimize switching losses, and enable soft switching;
3. Theoretical and simulation analysis was performed for various load conditions of the converter, including full load, half load, and light load with load regulation of the voltage, and current was also described;
4. To examine the controller performance, simulations were performed for variable input voltages with line regulation of load voltage, and current deviations were determined;
5. An experimental prototype for a 3.3 kW electric vehicle charger was demonstrated using GaN-HEMT technology;
6. Furthermore, the highlights of the entire theoretical, simulation, and experimental validations were discussed for steady-state and transient voltage and current ripples at the load side.

The organization of this paper is as follows. Section 1 presents the introduction and literature overview. Section 2 details the iL^2C resonant FB converter topology with the

working principle, followed by detailed analysis of the design parameters in Section 3. In Section 4, we discuss the proposed control strategy and present its detailed design. Section 5 provides the simulation results and various case studies, while experimental results and validation are detailed in Section 6. Section 7 presents the converter’s dynamic performance analysis under line and load regulations. Section 8 details the outcomes and conclusions of the proposed research work.

2. Interleaved L²C Resonant FB DC–DC Converter Topology and the Working Principle

A typical iL²C resonant FB DC–DC converter topology is shown in Figure 3 and key waveforms are presented in Figure 4. It consists of two resonant tanks, two switching circuits, and a single diode rectifier circuit [24]. The primary side employs two L²C resonant switching circuits called converter 1 and converter 2 connected in parallel, and secondary side is outfitted with two transformer secondary windings with a single rectifier network. The proposed technique provides operation in a phase shift angle of 180° of phase difference between the gate signals of converter 1 and converter 2, and the resonant frequency of the converter 1 is defined in Equation (1). Since the two converters’ operation is identical, all the equations and circuit operation are discussed for converter 1 with resonant network 1.

$$f_r = \frac{1}{2\pi\sqrt{L_r \times C_r}} \tag{1}$$

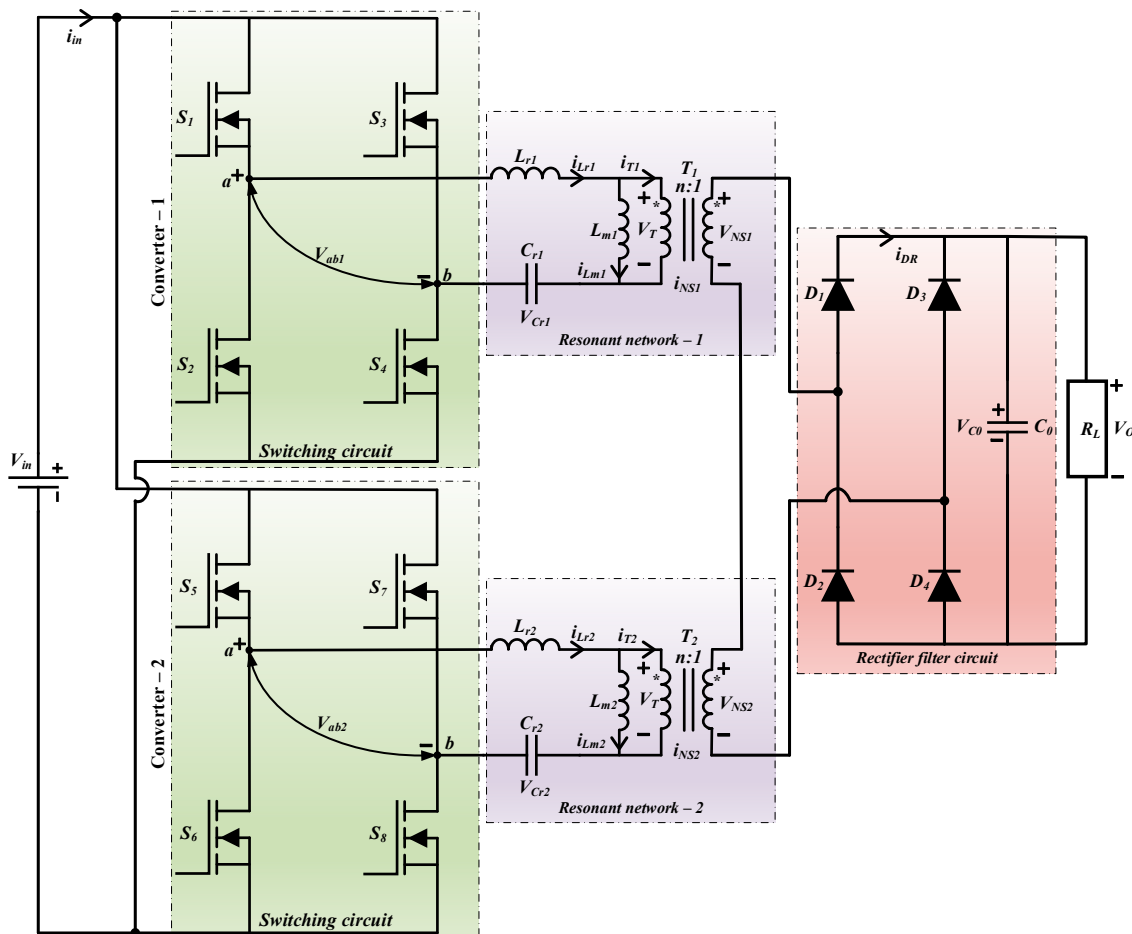


Figure 3. Typical structure of an iL²C resonant FB DC–DC power converter topology.

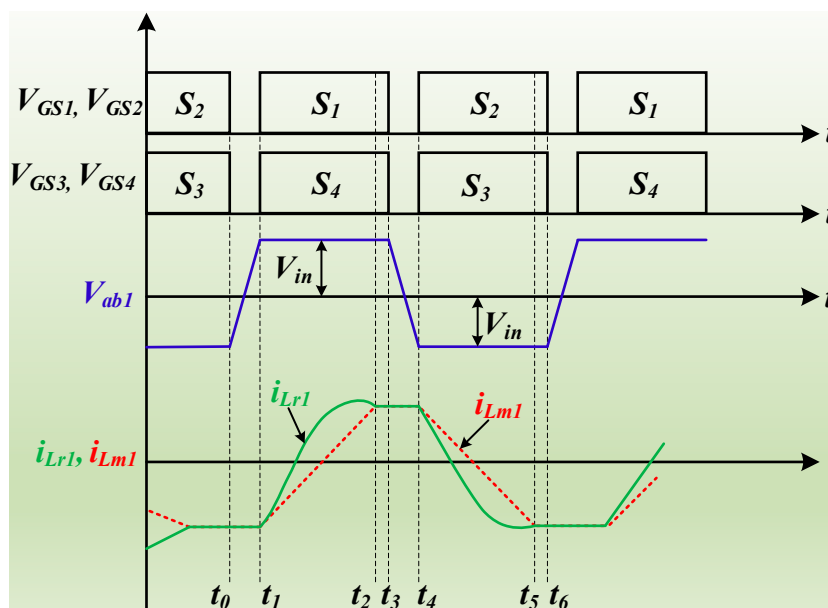


Figure 4. Key identical waveforms of iL^2C resonant FB DC-DC power converter 1.

Mode 1: Before t_0 , the switch S_2 and S_3 are turned ON with all the secondary side diodes in the OFF condition. At the point of t_0-t_1 , the switches S_2 and S_3 are turned OFF, and the body diodes of S_1 and S_4 are ON with the negative resonant current of i_{Lr1} .

Mode 2: During t_1-t_2 , the switch S_1 and S_4 are turned ON and the voltage V_{ab1} at transformer 1 T_1 is equal to input voltage V_{in} . The resonant inductor L_{r1} starts resonating with resonant capacitor C_{r1} ; meanwhile, filter capacitor C_0 is discharged through the secondary current of i_{NS1} . Additionally, diodes D_1 and D_4 are in the ON condition with the flow of current and voltage. The voltage at magnetizing inductance L_{m1} is defined in the following Equation (2) and the current across the i_{Lm1} increases linearly. At this period, the voltage at V_{NS1} is equal to the output voltage, which is defined in Equation (3),

$$L_{m1} = \frac{V_0}{n} \tag{2}$$

$$V_{NS1} = V_0 \tag{3}$$

The state space equation during stage 2 is defined in Equation (4) below:

$$\begin{cases} i_{Lr1}(t) = I_0 \cos(\omega_r t) + \frac{(nV_{in} - V_0 - nV_0)}{nZ_r} \sin(\omega_r t) \\ V_{Cr1}(t) = I_0 Z_r \sin(\omega_r t) + \left(V_0 + \frac{V_0}{n} - V_{in} \right) \cos(\omega_r t) \\ \quad + V_{in} - \frac{V_0 - V_{C0}}{n} \end{cases} \tag{4}$$

Mode 3: During the period t_2-t_3 , the switches S_1 and S_4 are turned OFF; due to the positive flow of the current at i_{Lr1} , the switches S_2 and S_3 are turned ON with all the secondary side diodes in the OFF condition.

Mode 4: During the period t_3-t_4 , the switches S_2 and S_3 are turned ON; because of negative current flow in i_{NS1} the secondary side diodes, D_2 and D_4 are ON. Therefore, the voltage at the secondary side of the transformer is defined by $-V_{C0}$ with very low voltage, and hence the current i_{Lm1} decreases linearly. The resonant inductor L_{r1} starts resonating with resonant capacitor C_{r1} ; meanwhile, filter capacitor C_0 is charged through the secondary current of i_{NS1} . At this period, the voltage V_{NS1} is given as follows:

$$V_{NS1} = -V_0 \tag{5}$$

The state space equation during stage 4 is defined in Equation (6) below:

$$\begin{cases} i_{Lr1}(t) = I_{Lr1}(t_2) \cos(\omega_r t) + \frac{(nV_{in} - V_0 - nV_{Cr1}(t_2))}{nZ_r} \sin(\omega_r t) \\ V_{Cr1}(t) = I_{Lr1}(t_2) Z_r \sin(\omega_r t) + \left(V_{Cr1}(t_2) - \frac{V_0}{n} - V_{in} \right) \cos(\omega_r t) \\ \quad + V_{in} + \frac{V_0}{n} \end{cases} \quad (6)$$

Mode 5: During the period t_4-t_5 , D_2 and D_3 are in the ON state with the secondary side transformer current i_{NS1} going to zero. The secondary side of the transformer voltage is denoted by Equation (7), and respective to that the magnetizing inductance decreases slowly. Furthermore, the resonant inductor L_{r1} starts resonating with the resonant capacitor C_{r1} .

$$V_{NS1} = -V_0 \quad (7)$$

The state space equation during stage 5 is defined in Equation (8) below:

$$\begin{cases} i_{Lr1}(t) = I_{Lr1}(t_4) \cos(\omega_r t) + \frac{(nV_{in} + V_0 - nV_{Cr1}(t_4))}{nZ_r} \sin(\omega_r t) \\ V_{Cr1}(t) = I_{Lr1}(t_4) Z_r \sin(\omega_r t) + \left(V_{Cr1}(t_4) - \frac{V_0}{n} - V_{in} \right) \cos(\omega_r t) \\ \quad + V_{in} + \frac{V_0}{n} \end{cases} \quad (8)$$

Mode 6: During the period t_5-t_6 , the secondary side of the transformer current i_{NS1} is completely zero with all the diodes in the OFF condition. At this period, the magnetizing inductance i_{Lm1} starts resonating with resonant capacitor C_{r1} and inductor L_{r1} .

After evaluating all the gains at peak values, we can define the ideal curve, as shown in Figure 5; if the frequency is 1, then the converter is operating at a resonance condition where $f_s = f_r$; likewise, if the frequency is less than 1, the converter is operating at below the resonance condition where $f_s < f_r$, and similarly, if the frequency is greater than 1, then the converter is operating above the resonance condition, where $f_s > f_r$ [31].

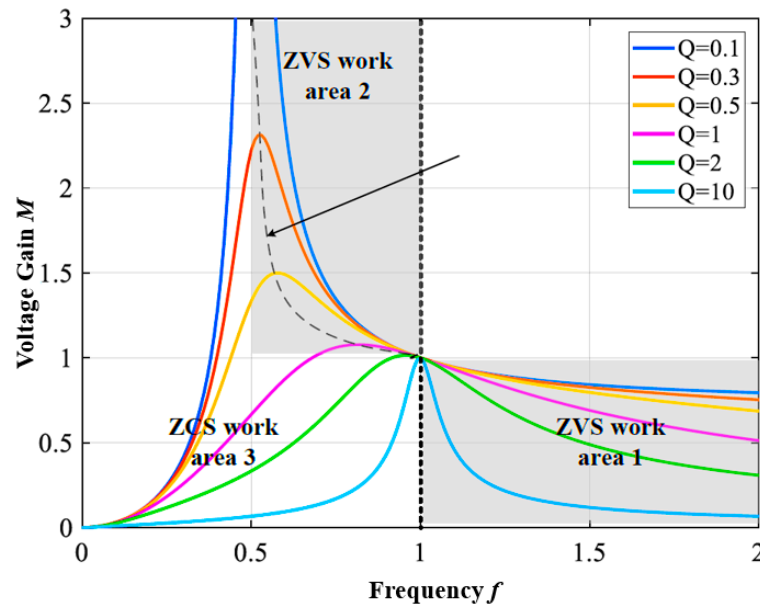


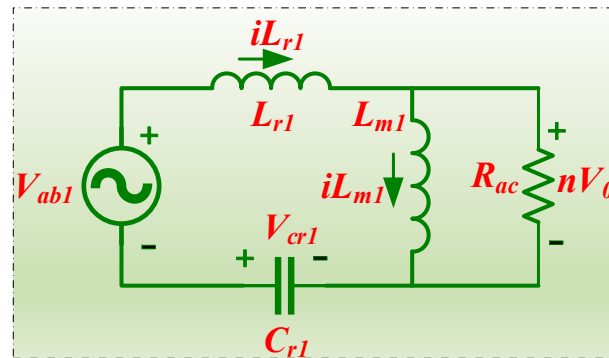
Figure 5. Voltage gain M vs. frequency f by varying the Q -factor.

3. Parameter Design

This section deals with the step-by-step design calculations of the iL^2C converter for all the components and their associated critical values [32]. Since converter 1 and converter 2 are identical in operation, the parametric design was calculated for converter 1. The main system parameters are shown in Table 1 and the AC equivalent circuit of LLC converter 1 is shown in Figure 6.

Table 1. Main parameters of an EV charger powered by an iL²C resonant DC–DC converter.

Parameter Description	Symbol	Electrical Value	Units
Minimum Input Voltage	V_{in_min}	300	Vdc
Maximum Input Voltage	V_{in_max}	500	Vdc
Rated Output Voltage	V_o	48	V
Rated Power	P	3300	W
Maximum Switching Frequency	f_{n_max}	$1.8 \times 150 = 270$	kHz
Maximum Switching Frequency	f_{n_min}	120	kHz
Resonant Frequency	f_r	150	kHz

**Figure 6.** Equivalent AC-circuit of LLC converter 1.

The transformer T_1 turning ratio and maximum and minimum values of the voltage gain of the iL²C converter at rated operating conditions are derived in Equations (9)–(11) [33,34].

$$n = \frac{V_{in_min}}{V_{0_min}} \quad (9)$$

$$M_{min} = \frac{n * V_{0_min}}{V_{in_max}} \quad (10)$$

$$M_{max} = \frac{n * V_{0_max}}{V_{in_min}} \quad (11)$$

where n is transformer turning ratio, V_{in_max} and V_{in_min} are maximum and minimum input voltages, V_{0_max} and V_{0_min} are maximum and minimum output voltages, and M_{max} and M_{min} are the maximum and minimum voltage gain.

The value of the inductor ratio L_{actual} is determined in the following Equation (12), where f_n represents the switching frequency. When the switching frequency is adjusted to the maximum value, the output from the previous step ensures that the converter enters the cut-off mode at the minimum output and maximum input [35].

$$L_{actual} = \left(\frac{1}{M_{min}} - 1 \right) \times \frac{8 \times f_{n_max}^2}{8 \times f_{n_max}^2 - \pi^2} \quad (12)$$

At the next step, we consider the resonant tank design of resonant inductance L_{r1} , capacitance C_{r1} , impedance Z_{01} , and magnetizing inductance L_{m1} with equivalent resistance R_{ac1} in the following Equations (13)–(17). The resonant inductor is derived from

Equation (12) and the magnetizing inductance of the converter. The equivalent resistance of the converter circuit is derived using Equation (13) followed by other critical equations.

$$R_{ac1} = \frac{8n^2}{\pi^2} \times R_L \quad (13)$$

$$L_{m1} = \frac{n^2}{f_r} \times \frac{V_{o_crit}}{4 * n * I_{sc} + [\pi^2 * L * M_{crit} - 4] * I_{o_crit}} \quad (14)$$

$$L_{r1} = L_{actual} \times L_{m1} \quad (15)$$

$$C_{r1} = \frac{1}{L_{r1} \times (2\pi f_r)^2} \quad (16)$$

$$Z_{01} = \sqrt{\frac{L_{r1}}{C_{r1}}} \quad (17)$$

The critical operating values of conversion gain M_{crit} , maximum impedance Z_0 , input current I_{in_crit} , output voltage V_{o_crit} , and current I_{o_crit} are determined in Equations (18)–(22), where P_{0_max} is the output power and η is the efficiency [36,37].

$$M_{crit} = \sqrt{1 + \sqrt{\frac{L}{1+L}}} \quad (18)$$

$$Z_{0_max} = \frac{8}{\pi^2} \times \frac{V_{in_min}^2}{P_{0_max}} \times \left[L + \sqrt{L(1+L)} \right] \quad (19)$$

$$V_{o_crit} = \frac{M_{crit} \times V_{in_min}}{n} \quad (20)$$

$$I_{o_crit} = \frac{P_{0_max}}{V_{o_crit}} \quad (21)$$

$$I_{in_crit} = \frac{P_{0_max}}{\eta * V_{in_min}} \quad (22)$$

The other important parametric Equations (23)–(27) are the quality factors of minimum Q_{min} and maximum Q_{max} , and the switching frequency of f_{n_max} and f_{n_min} , where R_{ac_max} and R_{ac_min} are the equivalent resistance of the maximum and minimum values, respectively, I_{in_max} is the input maximum current, and f_{n_max} and f_{n_min} are the switching frequency of the maximum and minimum values, respectively; further, f_{n_max} is 1.8 times the resonant frequency of f_r .

$$Q_{min} = \frac{Z_0}{R_{ac_max}} \quad (23)$$

$$Q_{max} = \frac{Z_0}{R_{ac_min}} \quad (24)$$

$$I_{in_max} = \frac{n \times V_{0_max}}{4 \times L_{m1} \times f_{r1}} \quad (25)$$

$$f_{n_min} = \left(1 - \frac{NI_{in_crit} - I_{o_crit}}{n * I_{s_max}} \right) \times f_r \quad (26)$$

$$f_{n_max} = 1.8 \times f_r \quad (27)$$

4. Hybrid Control Strategy

There are many control methods available currently in research on frequency modulation and phase shifting strategies, but in practice, they have their own drawbacks, namely, the converter has wide input and output voltage operations. In general, the phase shifting strategy is easy to design but complicated at wide input voltage ranges, and frequency modulation is an effective but complicated magnetic design. This paper proposes the combination of a hybrid control strategy named as the VFPSM technique for an iL^2C converter, which operates at all conditions with the same control strategy, unlike those in [25,26].

The generation of switching frequency f_s was carried out based on the provided error voltage by taking the output voltage V_o and comparing it with the reference input voltage V_{ref} . The comparison of input and output voltage references can be completed by using the Voltage Control Oscillator (VCO), which also drives the gate signals. The controller will control the output voltage V_o and vary the current, which is called the CV mode of operation, and the control circuit is shown in Figure 7. The design of the outer feedback compensator is greatly aided by the third-order transfer function mentioned in Equation (28), where the sub equations in the transfer function are discussed in Equations (29)–(33).

$$Gvf(s) = \frac{V(s)_0}{w(s)_s} = G_{dc} \frac{X_{eq}^2 + R_{eq}^2}{(s^2 L_e^2 + s L_e R_{eq} + X_{eq}^2) (1 + s R_L C_f) + R_{eq} (s L_e + R_{eq})} \quad (28)$$

$$L_e = L_r + \frac{1}{C_r \Omega_s^2} = L_r \left(1 + \frac{\Omega_0^2}{\Omega_s^2} \right) \quad (29)$$

$$R_{eq} = \frac{8}{\pi^2} n^2 R_L \quad (30)$$

$$X_{eq} = \Omega_s L_r - \frac{1}{\Omega_s C_r} \quad (31)$$

$$L_n = \frac{L_m}{L_r} \quad (32)$$

$$Q = \frac{\sqrt{\frac{L_r}{C_r}}}{n^2 R_L} \quad (33)$$

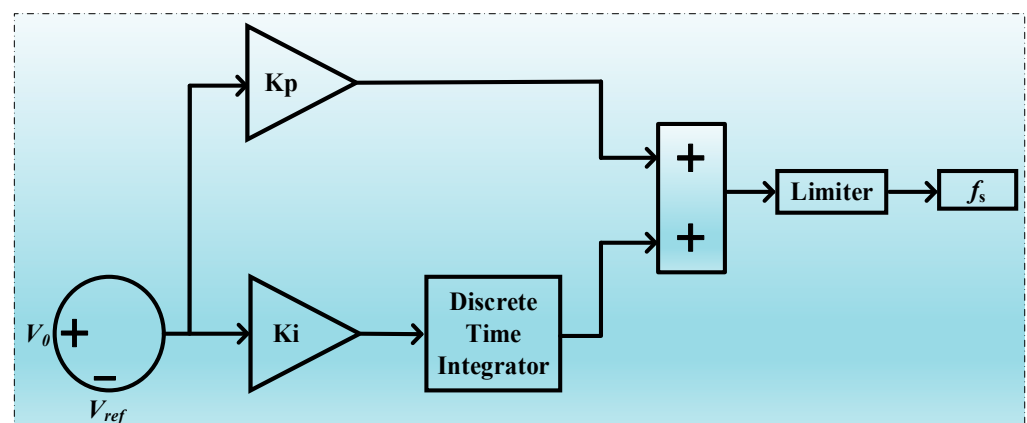


Figure 7. Voltage control oscillator block diagram for the constant voltage mode.

Generating the switching frequency from Figure 7 provides pulse generation to the switches. The phase shift of the 180° degree method was used to regulate the high input voltage over the broad range from 300–500 V_{in} and the VFPSM technique provided tight regulation of the line and load voltage and current. The switching operation of converter

1 and converter 2 is based on the phase shifting methodology termed as before 180° and after 180° , and the typical switching control circuit is shown in Figure 8.

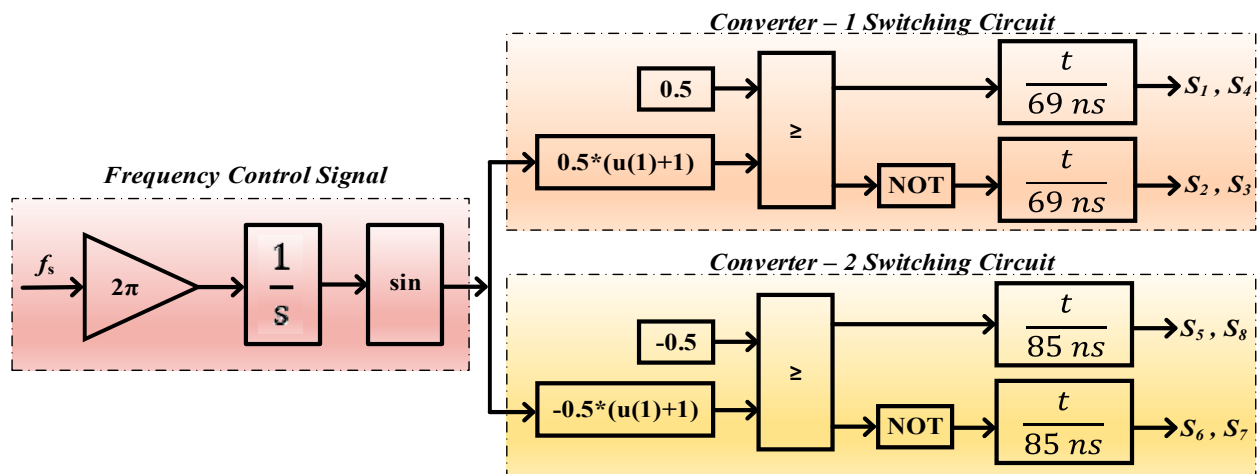


Figure 8. VFPSM control strategy control block diagram.

5. Simulation Results and Analysis

The simulation analysis was carried out in MATLAB/Simulink to check the performance of the proposed iL^2C converter with the VFPSM control technique. The actual design values of the converter were simulated and are tabulated in Table 2. The simulated analysis is presented for different case studies in the first case, and the nominal input and nominal output voltage at full load conditions were analyzed. In the next two cases, the converter was analyzed for half load and light load conditions at nominal voltage values; in addition to that, the load regulation of the voltage and current is presented. In the next step, two cases were performed to examine the hybrid controller: a variable step change in input voltages from $300\text{--}500 V_{in}$ and $500\text{--}300 V_{in}$ with a constant output voltage of $48 V_0$ at full load condition, which is discussed in terms of the line regulation of the load voltage and current.

Table 2. Modeling parameters of the iL^2C Converter.

Parameter Description	Symbol	Electrical Value	Units
Maximum Characteristic Impedance	Z_{o_max}	56.88	Ω
Characteristic Impedance	Z_o	20.83	Ω
Critical Voltage Gain	$M_{critical}$	1.311	V
Magnetizing Inductance	L_{m1}	20.55	μH
Minimum Equivalent Resistance	R_{ac1_min}	22.12	Ω
Maximum Equivalent Resistance	R_{ac1_max}	55.81	Ω
Resonant Inductor	L_{r1}	22.11	μH
Resonant Capacitor	C_{r1}	50.94	nF
Transformer Turns	n_1	8.82	-
Filter Capacitor	C_0	100	μF

5.1. Case 1: Performance Analysis of the Converter for a Nominal Input Voltage ($400 V_{in}$) with a Fixed Output Voltage ($48 V_0$) at Full Load Condition, i.e., 3.3 kW

This section analyzes the performance of the iL²C converter at a full load condition, i.e., 3.3 kW. Figure 9 shows the nominal input voltage of $400 V_{in}$ as the constant. The converter simulated results were examined with a controlled nominal load voltage and current of $48 V_0$ and 68.75 A at a full load condition, i.e., 3.3 kW, which is presented in Figure 10. The ripple voltage and currents were found with a voltage deviation of +0.5 V (+1.04%) at a rated output of $48 V_0$ and the current deviation is around +0.65 A (+0.94%) at a full load current of 68.75 A.

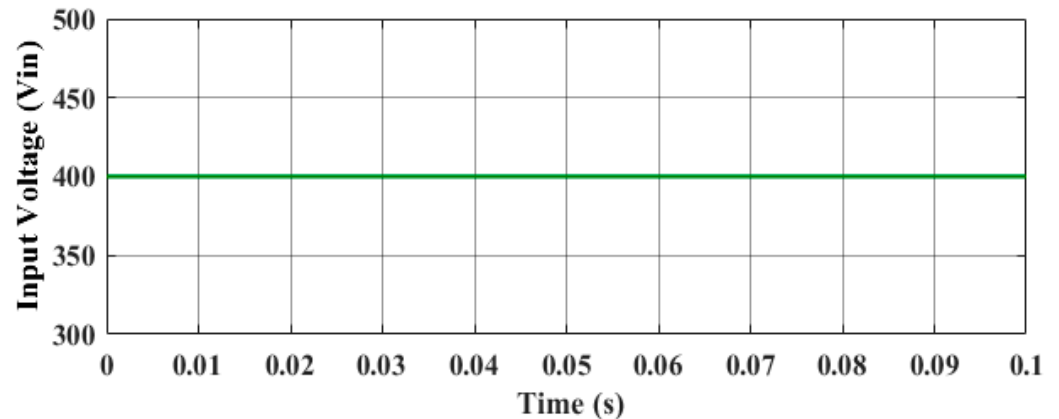


Figure 9. Nominal input voltage waveform ($V_{in} = 400 V$).

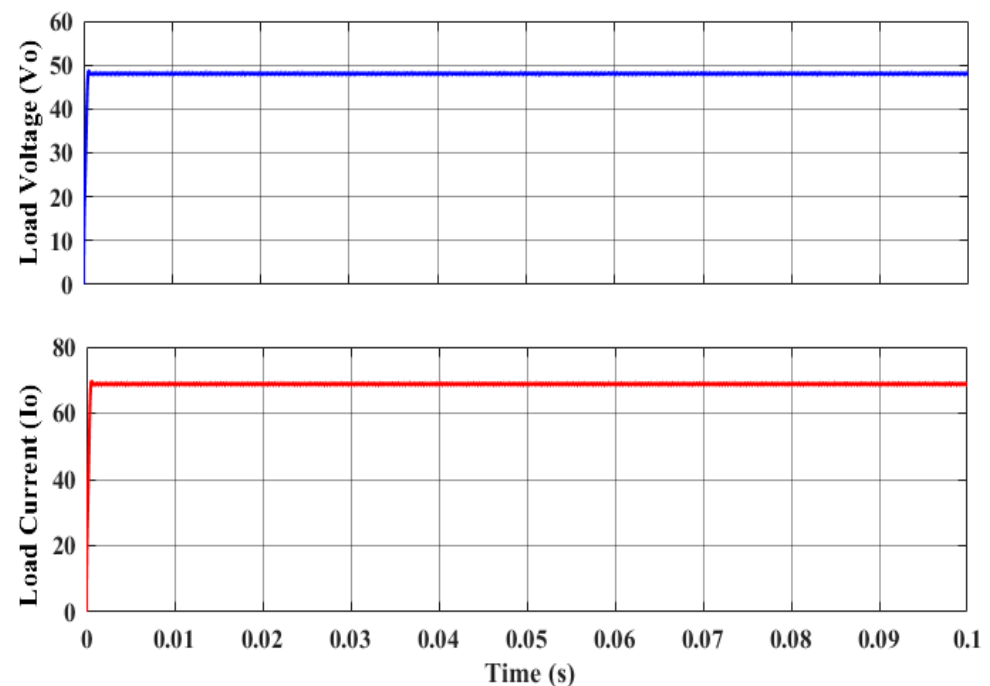


Figure 10. Load voltage and current waveforms ($V_0 = 48 V$, $I_0 = 68.75 A$).

5.2. Case 2: Performance Analysis of the Converter for a Nominal Input Voltage ($400 V_{in}$) with a Fixed Output Voltage ($48 V_0$) at a Half Load Condition, i.e., 1.65 kW

In this case, the converter operation was simulated at half of the load of the full load condition, which is at 1.65 kW. The nominal load voltage of $48 V_0$ and load current of 38.375 A at a half load condition are presented in Figure 11. The ripple voltage and currents were found with a voltage deviation of +0.3 V (+0.62%) at a rated output of $48 V_0$ and the current deviation was around +0.175 A (+0.5%) at a half load current of 38.375 A.

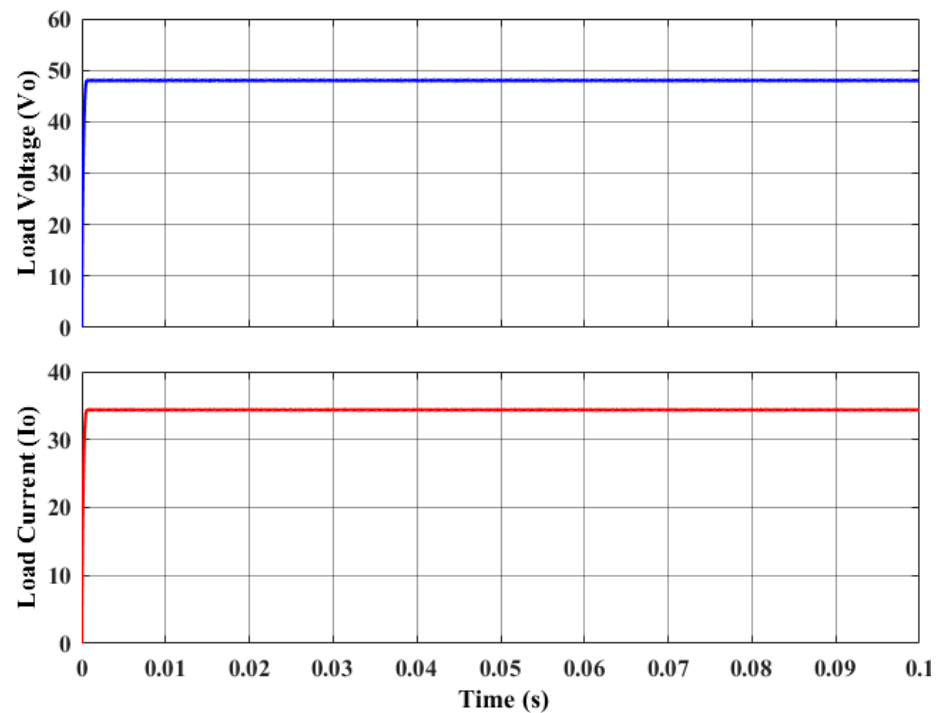


Figure 11. Load voltage and current waveforms ($V_0 = 48$ V, $I_0 = 38.375$ A).

5.3. Case 3: Performance Analysis of the Converter for a Nominal Input Voltage ($400 V_{in}$) with a Fixed Output Voltage ($48 V_0$) at a Light Load Condition, i.e., 0.33 kW

In this case, the converter operation was simulated at a light load, which is 10% of the full load condition, i.e., 330 W. The nominal load voltage of $48 V_0$ and the load current of 6.875 A at a light load condition are presented in Figure 12. The ripple voltage and currents were found with a voltage deviation of +0.15 V (+0.31%) at a rated output of $48 V_0$ and the current deviation was around +0.017 A (+0.25%) at a light load current of 6.875 A.

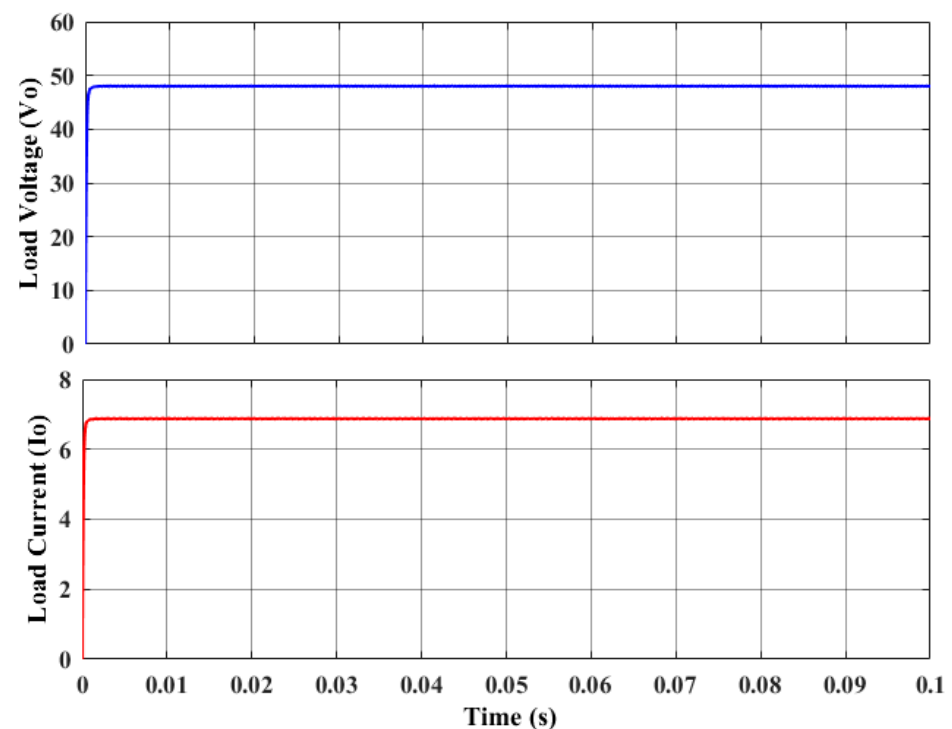


Figure 12. Load voltage and current waveforms ($V_0 = 48$ V, $I_0 = 6.875$ A).

5.4. Case 4: Performance Analysis of the Converter for a Variable Input Voltage (300–500 V_{in}) at a Fixed Output Voltage (48 V_0) at a Full Load Condition

This section analyzes the performance of the iL^2C converter for a variable input voltage of 300–500 V_{in} at a constant output voltage of 48 V_0 under a full load condition. Figure 13 shows that at 0.05 s, the voltage suddenly rose from 300 to 500 V_{in} ; the load voltage and load current waveforms are presented in Figure 14. During the transition of 300–500 V_{in} , the load voltage and current disturbances occurred at 0.05 s, and magnified figures are also presented. For the steady state voltage and current deviation of +0.4 V (+0.83%) and +0.59 A (+0.85%), a transient voltage and a current dip of +5.2 V (+10.83%) and +7.25 A (+10.54%) were found, respectively, and attained a load voltage of 48 V_0 within 1.1 ms.

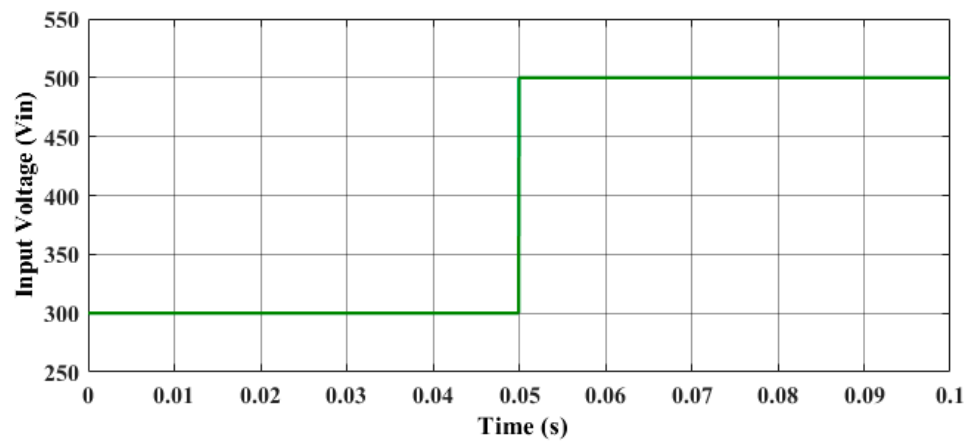


Figure 13. Variable input voltage waveform ($V_{in} = 300\text{--}500\text{ V}$) at 0.05 s.

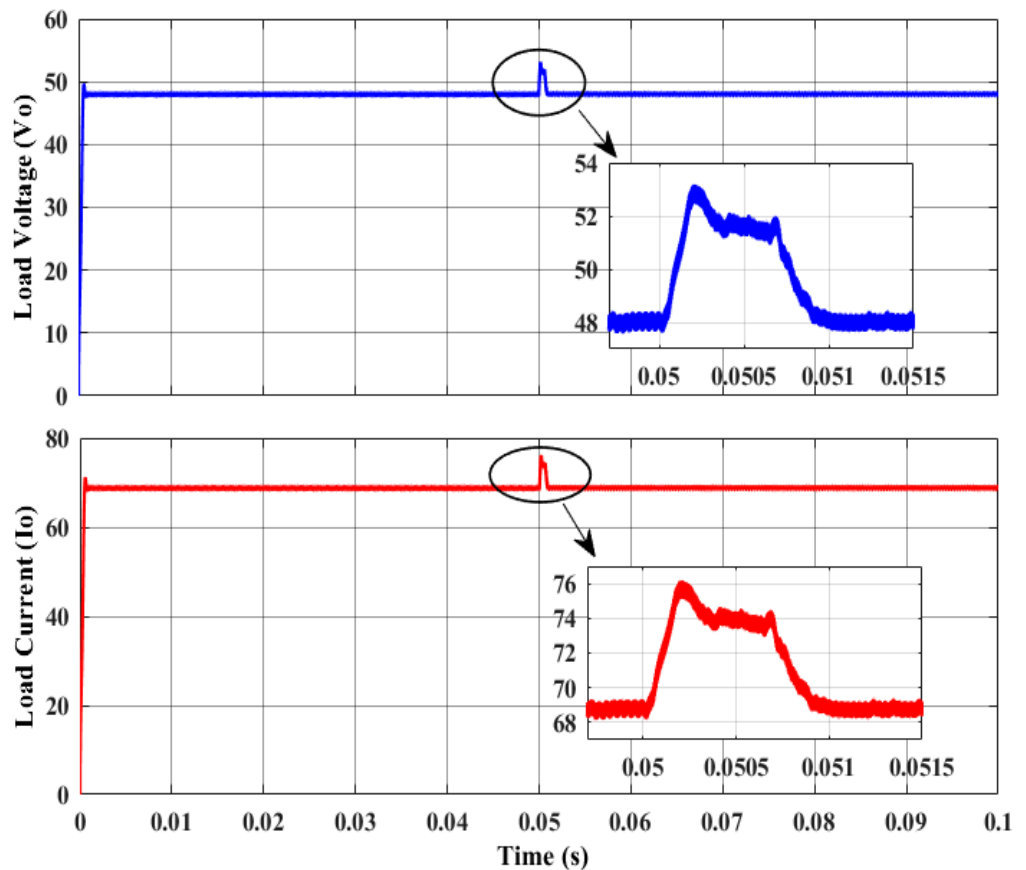


Figure 14. Step change in load voltage and current waveforms ($V_0 = 48\text{ V}$, $I_0 = 68.75\text{ A}$).

5.5. Case 5: Performance Analysis of the Converter for a Variable Input Voltage ($500\text{--}300V_{in}$) at a Fixed Output Voltage ($48V_0$) at a Full Load Condition

This section analyzes the performance of the iL^2C converter for a variable input voltage of $500\text{--}300V_{in}$ at a constant output voltage of $48V_0$ under a full load condition. Figure 15 shows that at 0.05 the voltage suddenly dropped from 500 to $300V_{in}$; load voltage and load current waveforms are presented in Figure 16. During the transition of $500\text{--}300V_{in}$, the load voltage and current disturbances occurred at 0.05 s, and magnified figures are also presented. For the steady state voltage and current deviation of $+0.42\text{ V}$ ($+0.875\%$) and $+0.64\text{ A}$ ($+0.93\%$), a transient voltage and current dip of -3.5 V (-7.29%) and -4.75 A (-6.9%) were found, respectively, and attained a load voltage of $48V_0$ within 1.2 ms.

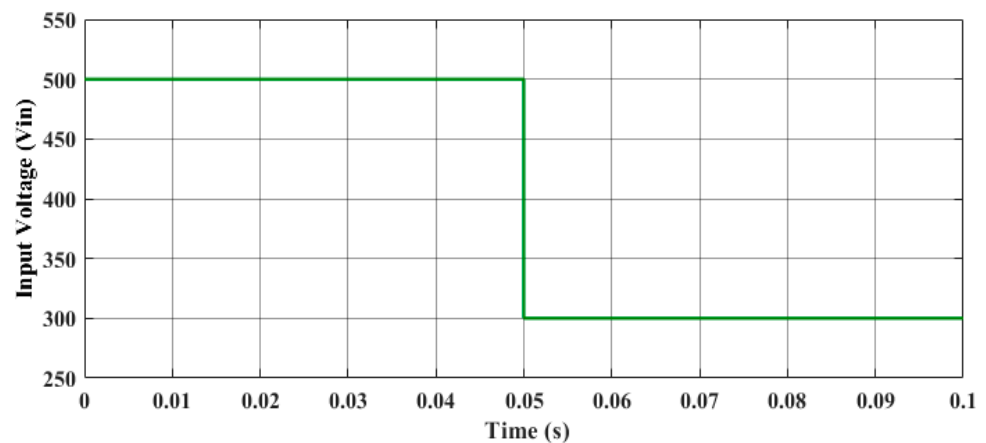


Figure 15. Variable input voltage waveform ($V_{in} = 500\text{--}300\text{ V}$) at 0.05 s.

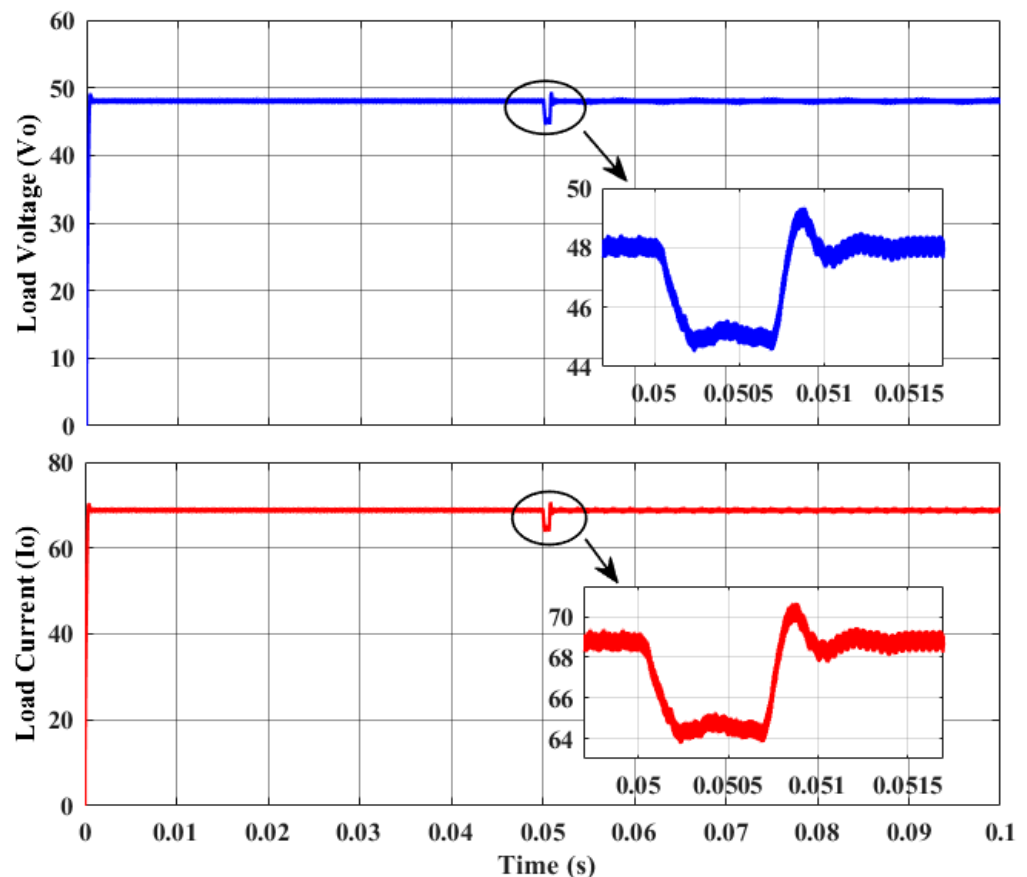


Figure 16. Step change in load voltage and current waveforms ($V_0 = 48\text{ V}$, $I_0 = 68.75\text{ A}$).

6. Experimental Analysis

This section describes the experimental validation of the iL^2C converter using GaN-HEMT technology at a full load condition of 3.3 kW with a variable input voltage of 300–500 V_{in} at a load voltage of 48 V_0 . Eight GaN-HEMT switches were utilized to operate the switching circuit; the parameters of the GaN switch GS66508T are presented in Table 3 and the manufacturer is GaN systems [38,39]. Its features include cooled technology with a lower-junction thermal case resistance at high power applications, lower on-state drain resistance, reverse recovery current, zero reverse recovery losses, well designed gate charge characteristics, and its enhancement mode (E-mode) transistor with better packaging capabilities, among others [40]. TMS320F28335 was used as a digital signal processor as the main controller for the iL^2C converter, and the prototype was built as per the modeling parameters discussed in Table 4.

Table 3. GaN GS66508T parameters (manufactured by GaN Systems).

Parameter Description	Symbol	Electrical Value	Units
Drain Source Voltage	V_{ds}	650	V
Continuous Drain Current	$I_{Ds(ON)}$	30	A
Drain Source Resistance	$R_{Ds(ON)}$	50	m Ω
Reverse Recovery Charge	Q_{RR}	0	nC
Total Gate Charge	Q_G	5.8	nC
Gate Drain Charge	Q_{GD}	1.8	nC
Gate Source Charge	Q_{GS}	2.2	nC
Turn ON Delay Time @125 °C	$t_{d(ON)}$	4.3	ns
Turn OFF Delay Time @125 °C	$t_{d(OFF)}$	8.2	ns
Internal Gate Resistance	R_G	1.1	Ω

Table 4. Practical prototype values of the iL^2C resonant FB DC–DC converter.

Parameter Description	Symbol	Electrical Value	Units
Variable Input Voltage	V_{in}	300–500	V
Rated Output Voltage	V_0	48	V
Rated Power	P	3300	W
Magnetizing Inductance	L_{m1} and L_{m2}	23	μ H
Resonant Inductors	L_{r1} and L_{r1}	21	μ H
Resonant Capacitors	C_{r1} and C_{r1}	56	nF
Transformer Turning Ratio	n_1 and n_2	8.82	-
Filter Capacitor	C_o	100	μ F

The hardware representation and experimental setup are presented in Figure 17. From Figure 18, the iL^2C converter was validated for 3.3 kW (load voltage 48 V_0 , load current 68.75 A) at variable load conditions.

The results were analyzed at T = 100 ms/div, load voltage = 20 V/div, denoted using a blue line, load current = 50 A/div, denoted using a pink line, and the input source voltage = 300 V/div, denoted using a red line. To perform the dynamic responses at the line side, the sudden change in input voltage occurred at 0.05 s (500 ms) with a small change in load voltage and the current was observed and marked, as shown in Figure 18. It is evident that the converter and controller performed as per the theoretical and simulation analysis. For the steady state voltage and current deviation of +0.76 V (+1.58%) and +1.38 A (+2.0%), a

transient voltage and current dip of +6.17 V (+12.85%) and +8.29 A (+12.05%) were found, respectively, and attained a load voltage of $48 V_0$ within 18 ms.

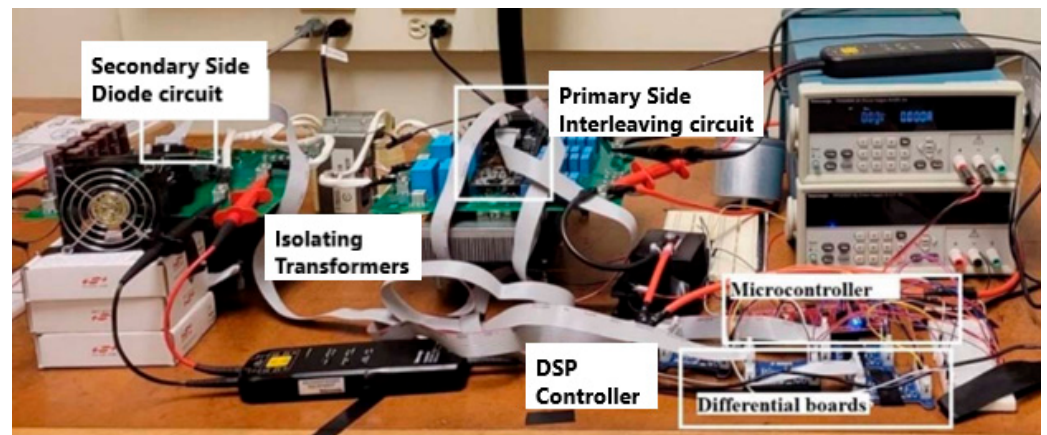


Figure 17. Test bench setup of the iL^2C resonant FB DC-DC converter at 3.3 kW.

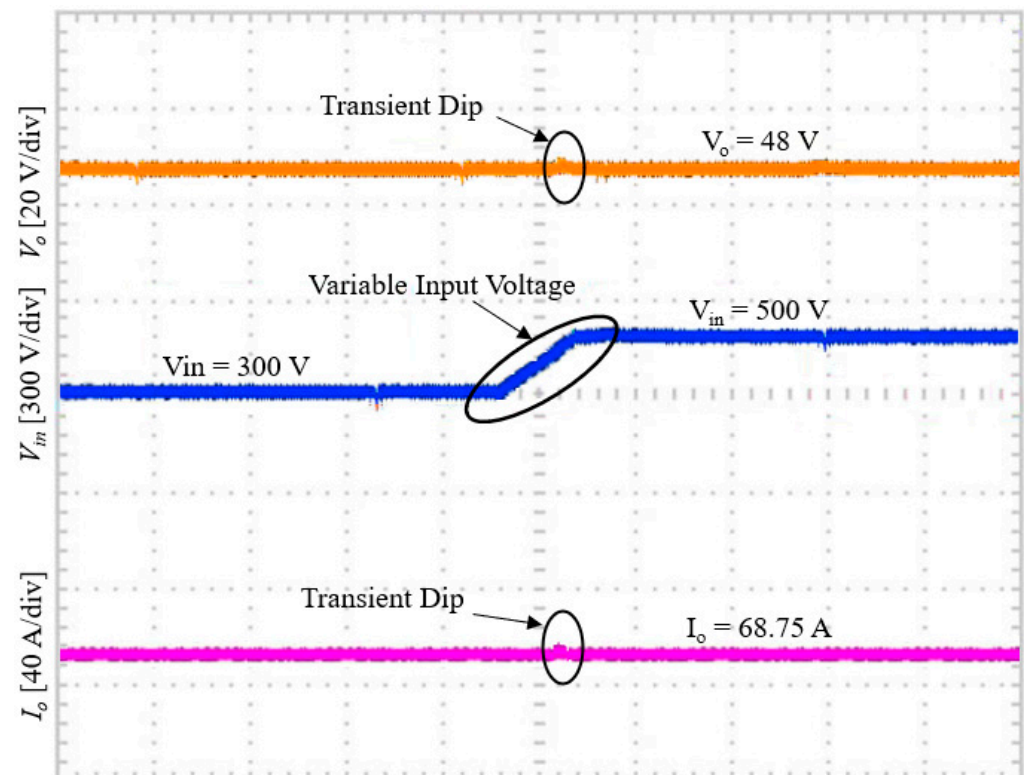
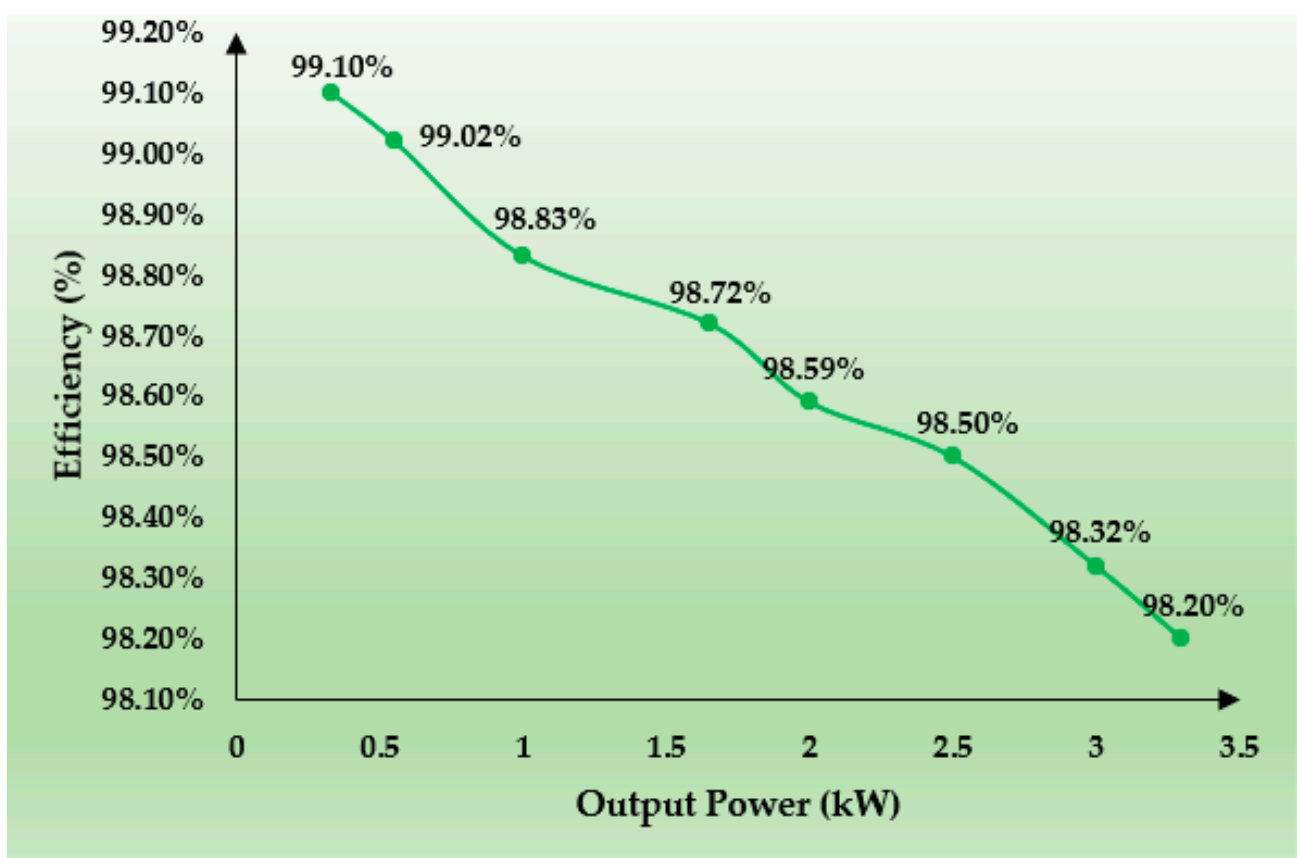


Figure 18. Experimental waveforms of variable input voltage ($V_{in} = 300\text{--}500\text{ V}$), load voltage, and load current ($V_0 = 48\text{ V}$, $I_0 = 68.75\text{ A}$).

The efficiency was measured during eight variable load conditions from full load to light load as summarized in Table 5, i.e., 3.3 kW, 3.0 kW, 2.5 kW, 2.0 kW, 1.65 kW, 1.0 kW, 0.5 kW, and 0.33 kW, respectively, when the input and output voltages were $400 V_{in}$ and $48 V_0$. The measured efficiency was 98.2%, 98.7%, and 99.1% at a full load of 3.3 kW, half load of 1.65 kW, and light load of 0.33 kW, respectively. Figure 19 shows the efficiency curve with regard to power.

Table 5. Efficiency vs. power at 400 V_{in} with a 48 V_0 .

No of Loads	Power (kW)	Efficiency (%)
1 (light load)	0.33	99.10
2	0.55	99.02
3	1.00	98.83
4 (half load)	1.65	98.72
5	2.00	98.59
6	2.50	98.50
7	3.00	98.32
8 (full load)	3.30	98.20

**Figure 19.** Efficiency vs. power.

7. Converter Analysis Tables

This section describes the steady state and transient deviations of the voltage and current in various simulated and experimentally analyzed case studies. The values were recorded in tabular format, and Tables 6 and 7 describe the voltage and current ripple in terms of full load (3.3 kW), half load (1.65 kW), and light load (0.33 kW). Tables 8 and 9 show the steady state and transient dip and ripples of the voltage and current during variable input voltages from 300 to 500 V_{in} and 500 to 300 V_{in} .

Table 6. Steady state analysis of the load voltage regulation at different load conditions.

Various Load Cases	Load Voltage	Voltage Ripple		Max. Load Voltage Deviation	Avg. %Load Voltage Ripple
		Minimum	Maximum		
Case 1: 3.30 kW	48 V	47.70 V	48.50 V	+0.50 V	+1.04%
Case 2: 1.65 kW	48 V	47.80 V	48.30 V	+0.30 V	+0.62%
Case 3: 0.33 kW	48 V	47.94 V	48.15 V	+0.15 V	+0.31%

Table 7. Steady state analysis of load current regulation at different load conditions.

Various Load Cases	Load Current	Current Ripple		Max. Load Current Deviation	Avg. %Load Current Ripple
		Minimum	Maximum		
Case 1: 3.30 kW	68.75 A	68.30 A	69.40 A	+0.650 A	+0.94%
Case 2: 1.65 kW	34.375 A	34.20 A	34.55 A	+0.175 A	+0.50%
Case 3: 0.33 kW	6.875 A	6.865 A	6.892 A	+0.017 A	+0.25%

Table 8. Steady state and transient analysis of load voltage during line regulation.

Variable Input Voltage	Steady State Voltage Ripple		Max. Load Voltage Deviation	Avg. %Load Voltage Ripple	Transient Analysis		
	Min	Max			Voltage Dip	Avg% of Dip	Settling Time
Case 4: 300–500 V	47.60 V	48.40 V	+0.40 V	+0.830%	+5.2 V	+10.83%	1.1 ms
Case 5: 500–300 V	47.70 V	48.42 V	+0.42 V	+0.875%	−3.5 V	−07.29%	1.2 ms

Table 9. Steady state and transient analysis of load current during line regulation.

Variable Input Voltage	Steady State Current Ripple		Max. Load Current Deviation	Avg. %Load Current Ripple	Transient Analysis		
	Min	Max			Current Dip	Avg% of Dip	Settling Time
Case 4: 300–500 V	68.2 A	69.34 A	+0.59 A	+0.85%	+7.25 A	+10.54%	1.1 ms
Case 5: 500–300 V	68.3 A	69.39 A	+0.64 A	+0.93%	−4.75 A	+06.90%	1.2 ms

From Table 6, the simulations were performed at different load conditions at a rated load voltage of 48 V₀ and a source of 400 V_{in} for examining the load voltage regulation. In case 1, with a minimum voltage ripple of 47.70 V and a maximum voltage ripple of 48.50 V with a load deviation of +0.50 V, the average percentage load voltage ripple was found to be +1.04%. In the next two cases, the minimum voltage ripple and maximum voltage ripple were generated at 47.80 V, 47.94 V and 48.30 V, 48.15 V, respectively. The load deviations occurred at +0.30 V and +0.15 V with an average percentage load voltage ripple of +0.62% and +0.31%, respectively.

Similarly, from Table 7, simulations were performed at different load conditions by maintaining the constant voltages of load 48 V₀ and source 400 V_{in} to examine the load current regulation. In case 1, for a minimum current ripple of 68.30 A and maximum current ripple of 69.40 A with a load deviation of +0.65 A, the average percentage of the load current ripple was found to be +0.94%. In the next two cases, the minimum current

ripple and the maximum current ripple were generated at 34.20 A, 6.865 A and 34.55 A, 6.892 A, respectively. The load deviations occurred at +0.175 A and +0.017 A with an average percentage load current ripple of +0.50% and +0.25%, respectively.

From Table 8, simulations were performed to examine the load voltage deviation for variable input voltages, i.e., 300–500 V_{in} and 500–300 V_{in} , by maintaining the load voltage at 48 V_0 and the load current at 68.75 A, respectively, at full load. In case 4 (300–500 V_{in}), for a minimum voltage ripple of 47.60 V and maximum voltage ripple of 48.40 V with a load deviation of +0.40 V, the average percentage of load voltage ripple was found to be +0.83%. The transient voltage dip was found to be +5.2 V and its average percentage dip was +10.83%, respectively, with a settling time of 1.1 ms. During case 5 (500–300 V_{in}), for a minimum voltage ripple of 47.70 V and a maximum voltage ripple of 48.42 V with a load deviation of +0.42 V, the average percentage of the load voltage ripple was found to be +0.875%. The transient voltage dip was found to be –3.5 V and its average percentage dip was –7.29%, respectively, with a settling time of 1.2 ms.

From Table 9, simulations were performed to examine the load current deviation for variable input voltages, i.e., 300–500 V_{in} and 500–300 V_{in} , by maintaining the load voltage at 48 V_0 and load current at 68.75 A, respectively, at full load. In case 4 (300–500 V_{in}), for a minimum current ripple of 68.2 A and a maximum current ripple of 69.34 A with a load deviation of +0.59, A the average percentage of load current ripple was found to be +0.85%. The transient current dip was found to be +7.25 A and its average percentage dip was +10.54%, respectively, with a settling time of 1.1 ms. During case 5 (500–300 V_{in}), for a minimum current ripple of 68.3 A and maximum current ripple of 69.39 A with a load deviation of +0.64 A, the average percentage of the load current ripple was found to be +0.93%. The transient current dip was found to be –4.75 A and its average percentage dip was –6.90%, respectively, with a settling time of 1.2 ms.

Finally, after experimental validation of the iL^2C converter's topology and the VFPSM control technique with a variable input voltage of 300 V_{in} –500 V_{in} at a full load of 3.3 kW ($V_0 = 48$ V & $I_0 = 68.75$ A), its use was verified and a comparative table is presented in Tables 10 and 11 in terms of line regulation for voltage and current at steady state and transient conditions respective to the simulations.

Table 10. Simulation vs. experimental analysis of load voltage deviations during line regulation from (300–500 V_{in}).

Conditions	Steady State Voltage Ripple		Max. Load Voltage Deviation	Avg. %Load Voltage Ripple	Transient Analysis		
	Min	Max			Voltage Dip	Avg% of Dip	Settling Time
Simulations	47.60 V	48.40 V	+0.40 V	+0.83%	+5.20 V	+10.83%	1.1 ms
Experimental	46.50 V	48.76 V	+0.76 V	+1.58%	+6.17 V	+12.85%	18 ms

From Table 10, in the case of experimental analysis, for a minimum voltage ripple of 46.50 V and maximum voltage ripple of 48.76 V with a load deviation of +0.76 V, the average percentage of load voltage ripple was found to be +1.58%. The transient voltage dip was found to be +6.17 V and its average percentage dip was +12.85%, respectively, with a settling time of 18 ms.

From Table 11, in the case of experimental analysis, for a minimum current ripple of 68.5 A and maximum voltage ripple of 70.13 A with a load deviation of +1.38 A, the average percentage of the load voltage ripple was found to be +2.00%. The transient voltage dip was found to be +8.29 A and its average percentage dip was +12.05%, respectively, with a settling time of 18 ms.

Table 11. Simulation vs. experimental analysis of load current deviations during line regulation from (300–500 V_{in}).

Conditions	Steady State Current Ripple		Max. Load Current Deviation	Avg. %Load Current Ripple	Transient Analysis		
	Min	Max			Current Dip	Avg% of Dip	Settling Time
Simulations	68.2 A	69.34 A	+0.59 A	+0.85%	+7.25 A	+10.54%	1.1 ms
Experimental	68.5 A	70.13 A	+1.38 A	+2.00%	+8.29 A	+12.05%	18 ms

8. Conclusions

An iL^2C Resonant FB DC–DC converter with a hybrid control strategy called the VFPSM technique with a wide input voltage for EV charging systems was investigated.

Firstly, the iL^2C converter was modeled and its working principle was demonstrated with the two-converter strategy, which increased the load capacity with a reduction in current ripples. To adapt the wide input voltage, tight regulation, and soft switching, a hybrid control strategy was proposed for the entire operating region, and its control loop design was discussed.

Simulations were conducted using MATLAB/Simulink for the entire proposed design. The converter performance was shifted in different case studies; during case 1, case 2, and case 3, the converter operated at different load conditions, i.e., full load (3.3 kW), half load (1.65 kW), and light load (10% of full load) with a constant input and load voltage of 400–48 V_0 . The steady-state analysis of load voltage and current regulation was determined with average percentage ripples. The converter's performance was also examined under assorted input voltage conditions from 300 to 500 V_{in} in case 4 and 500 to 300 V_{in} in case 5 at a full load condition. The load voltage and current deviations during line regulation were determined in terms of steady state and transient analysis.

Furthermore, to validate the converter and controller feasibility design, an experimental prototype was built for a 48 V_0 charging system with a variable input voltage of 300–500 V_{in} and implemented by using GaN-HEMT technology with an efficiency of 98.2% at full load. The steady-state and transient analysis of the proposed concept for voltage and current ripples at the load side was discussed.

Author Contributions: Conceptualization, R.P.N.; methodology, R.P.N.; software, R.P.N.; validation, R.P.N.; formal analysis, R.P.N. and S.M.; investigation, R.P.N.; writing—original draft preparation, R.P.N.; writing—review and editing, R.P.N.; supervision, S.M. All authors have read and agreed to the published version of the manuscript.

Funding: This research received no external funding.

Data Availability Statement: Not applicable.

Conflicts of Interest: The authors declare no conflict of interest.

Abbreviations

The abbreviations used in this paper are summarized as follows:

AC	Alternating Current
BEV	Battery Electric Vehicle
CV	Constant Voltage
DC	Direct Current
EMI	Electromagnetic Interference
E-mode	Enhancement mode
EV	Electric Vehicle
FB	Full Bridge
FCEV	Fuel cell Electric Vehicle

GaN	Gallium nitride
HEMT	High Electron Mobility Transistor
HEV	Hybrid Electric Vehicle
ICE	Internal Combustion Engine
iL ² C	Interleaved Inductor–inductor–capacitor
L ² C	Inductor–inductor–capacitor
PHEV	Plugin Hybrid Electric Vehicle
SCEV	Super Capacitor Electric Vehicle
Si	Silicon
UCEV	Ultra-Capacitor Electric Vehicle
VCO	Voltage Control Oscillator
VFPSM	Variable Frequency Phase Shift Modulation
ZCS	Zero Current Switching
ZVS	Zero Voltage Switching

References

- Mopidevi, S.; Narasipuram, R.P.; Aemalla, S.R.; Rajan, H. Emobility: Impacts and analysis of future transportation electrification market in economic, renewable energy and infrastructure perspective. *Int. J. Powertrains* **2022**, *11*, 264–284. [\[CrossRef\]](#)
- Zhou, K.; Wu, Y.; Wu, X.; Sun, Y.; Teng, D.; Liu, Y. Research and development review of power converter topologies and control technology for electric vehicle fast-charging systems. *Electronics* **2023**, *12*, 1581. [\[CrossRef\]](#)
- Shahjalal, M.; Shams, T.; Tasnim, M.N.; Ahmed, M.R.; Ahsan, M.; Haider, J. A critical review on charging technologies of electric vehicles. *Energies* **2022**, *15*, 8239. [\[CrossRef\]](#)
- Narasipuram, R.P.; Mopidevi, S. A technological overview & design considerations for developing electric vehicle charging stations. *J. Energy Storage* **2021**, *43*, 103225.
- Chakraborty, S.; Vu, H.-N.; Hasan, M.M.; Tran, D.-D.; Baghdadi, M.E.; Hegazy, O. DC-DC converter topologies for electric vehicles, plug-in hybrid electric vehicles and fast charging stations: State of the art and future trends. *Energies* **2019**, *12*, 1569. [\[CrossRef\]](#)
- Raghavendra, K.V.G.; Zeb, K.; Muthusamy, A.; Krishna, T.N.V.; Kumar, S.V.S.V.P.; Kim, D.-H.; Kim, M.-S.; Cho, H.-G.; Kim, H.-J. A comprehensive review of dc–dc converter topologies and modulation strategies with recent advances in solar photovoltaic systems. *Electronics* **2020**, *9*, 31. [\[CrossRef\]](#)
- Sayed, K.; El-Zohri, E.H.; Mahfouz, H. Analysis and design for interleaved ZCS buck DC-DC converter with low switching losses. *Int. J. Power Electron.* **2017**, *8*, 210–231. [\[CrossRef\]](#)
- Saleeb, H.; Sayed, K.; Kassem, A.; Mostafa, R. Control and analysis of bidirectional interleaved hybrid converter with coupled inductors for electric vehicle applications. *Electr. Eng.* **2020**, *102*, 195–222. [\[CrossRef\]](#)
- Lazar, J.F.; Martinelli, R. Steady-state analysis of the LLC series resonant converter. In Proceedings of the Sixteenth Annual IEEE Applied Power Electronics Conference and Exposition, Anaheim, CA, USA, 4–8 March 2001; Volume 2, pp. 728–735.
- Bai, H.; Zhang, Y.; Semanson, C.; Luo, C.; Mi, C.C. Modelling design and optimisation of a battery charger for plug-in hybrid electric vehicles. *IET Elect. Syst. Transp.* **2011**, *1*, 3–10. [\[CrossRef\]](#)
- Deng, J.; Li, S.; Hu, S.; Mi, C.C.; Ma, R. Design methodology of LLC resonant converters for electric vehicle battery chargers. *IEEE Trans. Veh. Technol.* **2014**, *63*, 1581–1592. [\[CrossRef\]](#)
- Beiranvand, R.; Rashidian, B.; Zolghadri, M.R.; Alavi, S.M.H. A design procedure for optimizing the LLC resonant converter as a wide output range voltage source. *IEEE Trans. Power Electron.* **2012**, *27*, 3749–3763. [\[CrossRef\]](#)
- Musavi, F.; Craciun, M.; Gautam, D.S.; Eberle, W.; Dunford, W.G. An LLC resonant DC-DC converter for wide output voltage range battery charging applications. *IEEE Trans. Power Electron.* **2013**, *28*, 5437–5445. [\[CrossRef\]](#)
- Narasipuram, R.P. Analysis, identification, and design of robust control techniques for ultra-lift Luo DC-DC converter powered by fuel cell. *Int. J. Comput. Aided Eng. Technol.* **2021**, *14*, 102–129. [\[CrossRef\]](#)
- Shi, B.; Yang, F.; Hu, C.; Ouyang, M. Modelling and improvement of oscillation problem in a double-sided LCC compensation network for electric vehicle wireless power transfer. *eTransportation* **2021**, *8*, 100108. [\[CrossRef\]](#)
- Sun, W.; Xing, Y.; Wu, H. Modified high-efficiency LLC converters with two split resonant branches for wide input-voltage range applications. *IEEE Trans. Power Electron.* **2017**, *33*, 7867–7879. [\[CrossRef\]](#)
- Kim, B.-C.; Park, K.-B.; Kim, C.-E.; Moon, G.-W. Load sharing characteristic of two-phase interleaved LLC resonant converter with parallel and series input structure. In Proceedings of the Energy Conversion Congress and Exposition (ECCE), San Jose, CA, USA, 20–24 September 2009; pp. 750–753.
- Gu, W.-J.; Harada, K. A new method to regulate resonant converters. *IEEE Trans. Power Electron.* **1988**, *3*, 430–439.
- Ahmad, A.; Khalid, M.; Ullah, Z.; Ahmad, N.; Aljaidi, M.; Malik, F.A.; Manzoor, U. Electric vehicle charging modes, technologies, and applications of smart charging. *Energies* **2022**, *15*, 9471. [\[CrossRef\]](#)
- Leijon, J.; Boström, C. Charging Electric vehicles today and in the future. *World Electr. Veh. J.* **2022**, *13*, 139. [\[CrossRef\]](#)
- Guo, B.; Zhang, Y.; Zhang, J.; Gao, J. Hybrid control strategy of phase-shifted full-bridge LLC converter based on digital direct phase-shift control. *J. Power Electron.* **2018**, *18*, 802–816.

22. Yoo, K.-M.; Lee, J.-Y. A 10-kW two-stage isolated/bidirectional dc/dc converter with hybrid-switching technique. *IEEE Trans. Ind. Electron.* **2013**, *60*, 2205–2213. [[CrossRef](#)]
23. Park, H.-P.; Jung, J.-H. Power stage and feedback loop design for LLC resonant converter in high switching frequency operation. *IEEE Trans. Power Electron.* **2017**, *32*, 7770–7782. [[CrossRef](#)]
24. Narasipuram, R.P. Modelling and simulation of automatic controlled solar input single switch high step-up DC-DC converter with less duty ratio. *Int. J. Ind. Electron. Drives* **2017**, *3*, 210–218.
25. Zhao, L.; Li, H.; Wu, X.; Zhang, J. An improved phase-shifted full-bridge converter with wide-range ZVS and reduced filter requirement. *IEEE Trans. Ind. Electron.* **2018**, *65*, 2167–2176. [[CrossRef](#)]
26. Long, X.; Chen, D. Small signal modeling of LLC converter with LED load and quasi-resonant controller based active ripple rejection. *Energies* **2023**, *16*, 3773. [[CrossRef](#)]
27. Liu, Z.; Li, B.; Lee, F.C.; Li, Q. High-efficiency high-density critical mode rectifier/inverter for wbg-device-based on-board charger. *IEEE Trans. Ind. Electron.* **2017**, *64*, 9114–9123. [[CrossRef](#)]
28. Keshmiri, N.; Wang, D.; Agrawal, B.; Hou, R.; Emadi, A. Current status and future trends of GaN HEMTs in electrified transportation. *IEEE Access* **2020**, *8*, 70553–70571. [[CrossRef](#)]
29. Musumeci, S.; Barba, V. Gallium Nitride Power Devices in Power Electronics Applications: State of Art and Perspectives. *Energies* **2023**, *16*, 3894. [[CrossRef](#)]
30. Sarnago, H.; Lucía, Ó.; Popa, I.O.; Burdío, J.M. Constant-Current Gate Driver for GaN HEMTs Applied to Resonant Power Conversion. *Energies* **2021**, *14*, 2377. [[CrossRef](#)]
31. Ma, C.-T. System planning of grid-connected electric vehicle charging stations and key technologies: A review. *Energies* **2019**, *12*, 4201. [[CrossRef](#)]
32. Nguyen, D.-D.; Bui, N.-T.; Yukita, K. Design and optimization of three-phase dual-active-bridge converters for electric vehicle charging stations. *Energies* **2020**, *13*, 150. [[CrossRef](#)]
33. Musavi, F.; Cracium, M.; Gautam, D.S.; Eberle, W. Control strategies for wide output voltage range LLC resonant DC-DC converters in battery chargers. *IEEE Trans. Veh. Technol.* **2014**, *63*, 1117–1125. [[CrossRef](#)]
34. Beiranvand, R.; Rashidian, B.; Zolghadri, M.R.; Alavi, S.M.H. Optimizing the normalized dead-time and maximum switching frequency of a wide-adjustable-range LLC resonant converter. *IEEE Trans. Power Electron.* **2011**, *26*, 462–472. [[CrossRef](#)]
35. Shahzad, M.I.; Iqbal, S.; Taib, S. Interleaved LLC converter with cascaded voltage-doubler rectifiers for deeply depleted pev battery charging. *IEEE Trans. Transp. Electrif.* **2018**, *4*, 89–98. [[CrossRef](#)]
36. Vu, H.-N.; Choi, W. A novel dual full-bridge LLC resonant converter for CC and CV charges of batteries for electric vehicles. *IEEE Trans. Ind. Electron.* **2018**, *65*, 2212–2225. [[CrossRef](#)]
37. Bing, L.; Wenduo, L.; Yan, L.; Lee, F.C.; van Wyk, J.D. Optimal design methodology for LLC resonant converter. In Proceedings of the Twenty-First Annual IEEE Applied Power Electronics Conference and Exposition, Dallas, TX, USA, 19–23 March 2006; pp. 533–538.
38. Ma, C.-T.; Yao, B.-H. Design and Implementation of an Integrated Control Scheme for GaN-Based Multiple Power Converters. *Micromachines* **2023**, *14*, 833. [[CrossRef](#)] [[PubMed](#)]
39. Lumberras, D.; Vilella, M.; Zaragoza, J.; Berbel, N.; Jordà, J.; Collado, A. Effect of the Heat Dissipation System on Hard-Switching GaN-Based Power Converters for Energy Conversion. *Energies* **2021**, *14*, 6287. [[CrossRef](#)]
40. Zulauf, G.; Park, S.; Liang, W.; Surakitbovorn, K.N.; Rivas-Davila, J. C_{OSS} Losses in 600 V GaN power semiconductors in soft-switched, high- and very-high-frequency power converters. *IEEE Trans. Power Electron.* **2018**, *33*, 10748–10763. [[CrossRef](#)]

Disclaimer/Publisher’s Note: The statements, opinions and data contained in all publications are solely those of the individual author(s) and contributor(s) and not of MDPI and/or the editor(s). MDPI and/or the editor(s) disclaim responsibility for any injury to people or property resulting from any ideas, methods, instructions or products referred to in the content.